

# Optical phonons of graphene and nanotubes

S. Piscanec<sup>1</sup>, M. Lazzeri<sup>2</sup>, F. Mauri<sup>2</sup>, and A.C. Ferrari<sup>1,a</sup>

<sup>1</sup> Engineering Department, Cambridge University, 9 JJ Thomson Avenue, Cambridge CB3 0FA, UK

<sup>2</sup> IMPMC, Universités Paris 6 et 7, CNRS, IPGP, 140 rue de Lourmel, 75015 Paris, France

**Abstract.** We review the optical phonon dispersions of graphene. In particular, we focus on the presence of two Kohn anomalies in the highest optical phonon branch at the  $\Gamma$  and  $\mathbf{K}$  points of the Brillouin zone. We then show how graphene can be used as a model for the calculation of phonons in carbon nanotubes. Finally, we present the beyond Born-Oppenheimer corrections to their phonon dispersions. These are experimentally revealed in the Raman spectra of doped samples.

## 1 Introduction

Graphene is a bi-dimensional crystal of carbon atoms arranged into a honeycomb lattice. Even before its recent discovery in the free state [1,2], graphene was widely employed as a toy model for the description of the electronic and vibrational properties of other form of  $sp^2$  bonded carbons, like graphite and carbon nanotubes [3–5].

Here we review the vibrational properties of graphene, showing how its phonon dispersion is shaped by the effects of electron–phonon interaction, which results in the presence of two Kohn anomalies in the highest optical branch.

We then show how graphene can be used to accurately compute the phonon frequencies of single wall carbon nanotubes (SWNTs). In particular, we emphasize the description of the Kohn anomalies in the phonon dispersion of metallic SWNTs, underlying how their correct description can be achieved only by considering the time-dependent nature of phonons. Finally we discuss the Raman signatures of adiabatic and non-adiabatic Kohn anomalies in the Raman spectra of graphene and metallic nanotubes.

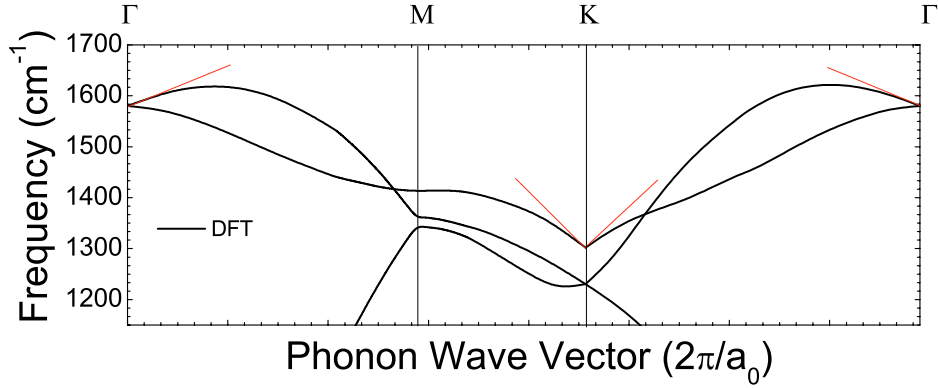
## 2 Optical phonons of graphene

Figure 1 presents the high frequency region of the phonon dispersion of graphene, as obtained by density functional theory calculations in [6]. Calculations are performed within the generalized gradient approximation (GGA) [7], using the density functional perturbation theory (DFPT) scheme [8], which allows the exact (within DFT) computation of phonon frequencies at any Brillouin Zone (BZ) point. We use plane-waves (90 Ry cut-off) and pseudopotential [9] approaches. We treat the semi-metallic character of the system by performing the electronic integration with a smearing technique [10], i.e. occupying the electronic levels according to a distribution with a finite *fictitious* electronic temperature  $\sigma$ . This smears out the discontinuities present in the Fermi distribution for  $\sigma=0$ . Calculations are performed at the experimental lattice spacing ( $a_0 = 2.46 \text{ \AA}$ ). Graphene layers are separated by  $7.4 \text{ \AA}$  of vacuum.

The most striking feature of the dispersion in figure 1 is the discontinuity in the frequency derivative of the highest optical branches (HOB) at  $\Gamma$  and at  $\mathbf{K}$  ( $E_{2g}$  and  $A'_1$  modes). This

---

<sup>a</sup> e-mail: acf26@eng.cam.ac.uk



**Fig. 1.** Phonon dispersion of graphene calculated by DFPT. The red lines are guide for the eye, emphasizing the presence of the two Kohn anomalies at  $\Gamma$  and  $\mathbf{K}$ .

discontinuity, emphasized by the red lines in figure 1, is strongly related to the metallic nature of graphene. Indeed, the two cusps can be observed only if the calculations are strictly converged with respect to the electronic smearing. Within DFPT, the smearing  $\sigma$  affects virtual transitions between occupied and empty states, differing in energy by  $\sim \sigma$ . This proves that the discontinuity are related to an anomalous screening of the electrons around the Fermi energy, and are thus Kohn anomalies [11].

In general, atomic vibrations are partially screened by electronic states. In a metal this screening can change rapidly for vibrations associated to certain  $\mathbf{q}$  points, entirely determined by the shape of the Fermi surface. The consequent anomalous behavior of the phonon dispersion is called Kohn anomaly [11]. Kohn anomalies may occur only for wavevectors  $\mathbf{q}$  such that there are two electronic states  $\mathbf{k}_1$  and  $\mathbf{k}_2 = \mathbf{k}_1 + \mathbf{q}$  both on the Fermi surface [11]. In graphene, the gap between occupied and empty electronic states is zero at  $\mathbf{K}$  and  $\mathbf{K}'$ . Since  $\mathbf{K}' = 2\mathbf{K}$ , these are connected by the vector  $\mathbf{K}$ . Thus, Kohn anomalies can occur for  $\mathbf{q} = \Gamma$  or  $\mathbf{q} = \mathbf{K}$ , as shown in figure 1.

The  $\mathbf{q} = \Gamma$  or  $\mathbf{q} = \mathbf{K}$  cusps cannot be described by a finite set of interatomic force constants or by a set decaying exponentially with the real-space distance. Indeed, if they decayed exponentially, the dependence of the dynamical matrix on the reciprocal space vectors would be analytic, and, because of symmetry, the highest optical branch near  $\Gamma$  and  $\mathbf{K}$  would have a flat slope. Thus, the two discontinuities indicate a non-analytic behavior of the phonon dispersion, due to a polynomial decay of the force constants in real space. This explains why it is impossible for any of the often used few-nearest-neighbors force constants approaches to properly describe the HOB phonons near  $\mathbf{K}$  and  $\Gamma$  [6].

Interestingly for a given value of  $\mathbf{q}$ , the Kohn anomalies are present only in the highest optical branches. This can be understood by noting that the non-analyticities of the dynamical matrix are due to terms proportional to the electron-phonon coupling. Thus, only phonons with a non-zero electron-phonon coupling matrix element (EPC) for transitions close to the Fermi energy can be affected by the Kohn anomalies. An explicit calculation of the EPC for the modes of graphene at  $\Gamma$  and  $\mathbf{K}$  clearly shows that this condition is satisfied by the highest optical branches only [6, 12, 13, 15].

Starting from the adiabatic expression of the dynamical matrix, and describing the electron-phonon coupling with a first neighbor tight binding model, it is possible to derive an entirely analytical description of the Kohn anomalies in graphene [6]. Defining  $\langle D_{\Gamma}^2 \rangle_F = \sum_{i,j}^{\pi} |D_{\mathbf{k}i,\mathbf{k}j}|^2/4$ , where the sum is on the two degenerate  $\pi$  bands at the Fermi level  $\epsilon_F$  and  $D_{(k+q)i,kj} = \langle k+q, i | \Delta V_q | k, j \rangle$  is the electron-phonon coupling (EPC) matrix element, with  $|\mathbf{k}, i\rangle$  the electronic Bloch eigenstate of wavevector  $\mathbf{k}$ , band  $i$ , energy  $\epsilon_{k,i}$ , and occupation  $f_{k,i}$  given by the Fermi-Dirac distribution function;  $\Delta V_q$  is the derivative of the electronic potential with respect to a displacement along the phonon normal coordinate. In particular, we have shown that the slope of the phonon dispersion at  $\Gamma$  and  $\mathbf{K}$  is proportional to the square of the electron-phonon

coupling and inversely proportional to the Fermi velocity [6,12,13,15]:

$$S_{\Gamma}^{\text{LO}} = \frac{\sqrt{3}\hbar a_0^2}{8M\omega_{\Gamma}\beta} \langle D_{\Gamma}^2 \rangle_F, \quad (1)$$

and

$$S_{\mathbf{K}}^{\text{TO}} = \frac{\sqrt{3}\hbar a_0^2}{8M\omega_{\mathbf{K}}\beta} \langle D_{\mathbf{k}}^2 \rangle_F, \quad (2)$$

where  $\beta = \hbar v_F = 5.52 \text{ \AA eV}$  is the slope of the electron bands near  $\epsilon_F$ ,  $v_F$  is the Fermi velocity,  $M$  is the carbon atomic mass,  $\omega_{\Gamma}$  is the frequency of the  $E_{2g}$  phonon ( $\hbar\omega_{\Gamma} = 196.0 \text{ meV}$ ),  $\omega_{\mathbf{K}}$  is the frequency of the  $\mathbf{K}-A'_1$  phonon.

The experimental phonon dispersions can then be used to measure the EPC matrix elements. In particular, our calculated DFT values are experimentally confirmed. E.g., let's consider the EPC relative to the  $E_{2g}$  phonon at  $\Gamma$ . The  $\Gamma$ - $E_{2g}$  mode is doubly degenerate and consists of an antiphase in-plane motion. For a small non zero  $\mathbf{q}$  near  $\Gamma$ , this splits into a quasi longitudinal (LO) and quasi transverse (TO) branch, corresponding to an atomic motion parallel and perpendicular to  $\mathbf{q}$ . From DFT calculations we get  $\langle D_{\Gamma}^2 \rangle_F = 45.60 (\text{eV}\text{\AA}^{-1})^2$  for both LO and TO modes [6]. The shape of the phonon branches around  $\Gamma$ , which are the best determined experimentally, is well reproduced by our calculations [6,12,13]. From a quadratic fit to the most recent data of [15] we get  $S_{\Gamma}^{\text{LO}} = 133 \text{ cm}^{-1} \text{ \AA}$ . From equation (1) we have  $\langle D_{\Gamma}^2 \rangle_F = 39 (\text{eV}\text{\AA}^{-1})^2$ , in good agreement with DFT.

### 3 Optical phonons in nanotubes

#### 3.1 Adiabatic Kohn anomalies

Graphene can be used as a model for the calculation of the electronic and vibrational properties of carbon nanotubes. A SWNT can be thought as rolled up graphene [3,4]. The chirality of a SWNT is determined by the length and orientation of the vector identifying its diameter on a graphene sheet [3,4]. Depending on its chirality, a SWNT can be either metallic or semiconducting. The differences between graphene and SWNTs can be explained in terms of curvature and confinement [13]. Curvature effects arise because in a non planar geometry the C-C bonds assume a mixed  $\sigma - \pi$  character. Confinement effects arise because the electronic wave-functions in a SWNT have to be commensurate to the tube circumference, resulting in the quantization of the electronic momentum component perpendicular to the tube axis.

Neglecting the effects of curvature, it is thus possible to map the electronic states of SWNT onto those of graphene. It has been shown that folding the electronic structure of graphene to describe the band structure of SWNTs produces accurate results for tubes larger than 0.8 nm [16]. This technique is known as *electronic zone folding* (EZF). In the past, a similar technique had also been applied to phonons. This goes under the name of *phonon zone folding* (PZF). However, as discussed in section 2, the phonon dispersions of graphene are affected by two Kohn anomalies, which occur only in metals. Thus, Kohn anomalies cannot be present in semiconducting SWNTs, while they will be enhanced in metallic SWNTs because of their reduced dimensionality [12,13]. As a consequence, PZF is not suitable for the description of the phonon dispersion of SWNTs close to the Kohn anomalies. However, neglecting the effects of confinement, the phonons of SWNTs can be obtained from the phonons of a flat graphene sheet, if the calculation is done performing the electronic Brillouin-zone integration on the lines of the electronic zone-folding [12,13]. This approach allows the description of all the effects of confinement, and can be used to compute the phonon dispersions of tubes with a diameter larger than 0.8 nm, i.e. those typically used in experiments.

#### 3.2 Non-adiabatic Kohn anomalies

Things change if non-adiabatic effects are taken in account [13,17,18]. Indeed, the techniques used for the computation of phonons in graphene and carbon nanotubes (DFPT, frozen

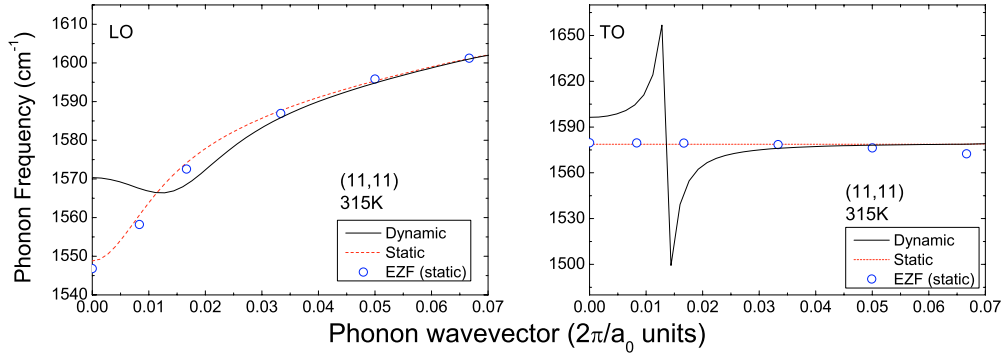


**Fig. 2.** Shape of the phonon dispersion of the modes derived from graphene  $E_{2g}$  for a (11,11) SWNT. Blue dots are the result of static EZF calculations. The red dotted line and the blue continuous line are obtained with an analytic model based respectively on the adiabatic and non-adiabatic description of phonons.

phonons) are based on the adiabatic Born-Oppenheimer approximation [19]. Thus, the motion of the electrons is assumed to be entirely decoupled from the motion of the ions, and phonons can be described as time independent perturbations. This approach, which for tri-dimensional metals produces excellent results [20], fails in the description of the vibrational properties of SWNTs, because of their reduced dimensionality.

Within a time-dependent approach, the reciprocal-space expression for the non-analytic part of the dynamical matrix of SWNTs,  $\tilde{\Theta}_q$  is given by [13,21]:

$$\tilde{\Theta}_q = \frac{2\tau A_{\Gamma/K}}{2\pi} \int_{-\bar{k}}^{\bar{k}} |D_{(K+k'+q)\pi^*,(K+k')\pi}|^2 \frac{f_{K+k,\pi} - f_{K+k'+q,\pi^*}}{\epsilon_{K+k',\pi} - \epsilon_{K+k'+q,\pi^*} + \hbar\omega_q + i\gamma} dk', \quad (3)$$

where  $\tau$  is the length of the translational unit of the tube,  $k'$  is measured from the Fermi point  $k_F$ ;  $\bar{k}$  has a small but finite value;  $A_{\Gamma/K}$  accounts for the number of processes satisfying  $2q = k_F$  ( $A_{\Gamma} = 2$ ,  $A_K = 1$ ),  $\hbar\omega_q$  is the energy of a phonon of wavevector  $q$  and branch  $\eta$  (omitted in the equations for simplicity),  $\gamma$  is a small real number. Within the adiabatic approximation, the phonon is described in its static limit, which corresponds to assuming  $\omega_q = 0$  and  $\gamma = 0$ . The expression for of  $\tilde{\Theta}_q$  thus simplifies as:

$$\tilde{\Theta}_q = \frac{2A_{\Gamma/K}\tau}{2\pi} \int_{-\bar{k}}^{\bar{k}} \frac{f_{K+k',\pi} - f_{K+k'+q,\pi^*}}{\epsilon_{K+k',\pi} - \epsilon_{K+k'+q,\pi^*} - i\gamma} |D_{(K+k'+q)\pi^*,(K+k')\pi}|^2 \cdot dk'. \quad (4)$$

Kohn Anomalies occur for phonons (i) having non-zero EPC between states close to the Fermi energy, and (ii) for which the denominator in equations (3), (4) vanish, resulting in the presence of a singularity in the dynamical matrix [6]. Thus, within a static approach, the anomalies are predicted to occur for the values of  $q$  that make the denominator in equation (4) vanish, i.e. for  $q = 0$  and  $q = 2k_F$  [6,12,22,23].

The non-adiabatic approach leads to a deep modification in the description of the Kohn anomalies. Because of the presence of the  $\hbar\omega_q + i\gamma$  terms, and assuming the electronic bands of the SWNTs at the Fermi energy to be linear with slope  $\beta$ , the denominator of equation (3) vanishes for  $q = \pm\hbar\omega_q/\beta$  and  $q = k_F \pm \hbar\omega_q/\beta$ , resulting in a shift of the position of the KAs.

Using the folding approach described in [12,13], it is easy to numerically integrate equations (3), (4), and obtain the theoretical description of the KAs in metallic SWNTs within the adiabatic (static) and non-adiabatic (dynamic) approaches. These results should then be corrected for the curvature effects, as described in [13].

Figure 2 compares the the modes derived from the graphene  $E_{2g}$  in a (11,11) metallic SWNTs, calculated using a static and a dynamic description of the phonons. In the first case only the LO mode is affected by a Kohn anomaly, centered at  $\mathbf{q} = \Gamma$ . On the other hand, calculations performed with the dynamic, time-dependent approach show the presence of

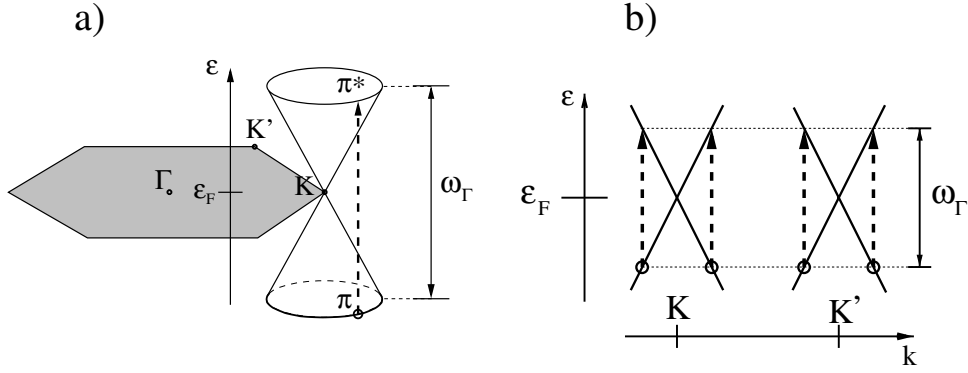


**Fig. 3.** Electron bands around  $\mathbf{K}$  in graphene (a) and in a metallic tube (b). Shaded area is the graphene Brillouin zone. Dashed arrows: decay processes for a  $\Gamma$  phonon.

the anomalies for both the LO and the TO modes, and predict the anomalies to be shifted from  $\Gamma$  [13].

#### 4 Phonon linewidths in graphene and nanotubes

In a perfect crystal, the linewidth  $\gamma$  of a phonon is determined by its interaction with other elementary excitations. Usually,  $\gamma = \gamma^{an} + \gamma^{EP}$ , where  $\gamma^{an}$  is due to the interaction with other phonons and  $\gamma^{EP}$  to the interaction with electron-hole pairs.  $\gamma^{an}$  is determined by anharmonic terms in the interatomic potential and is always present.  $\gamma^{EP}$  is determined by the EPC, and is present only in systems where the electron gap is zero. If the anharmonic contribution  $\gamma^{an}$  is negligible or otherwise known, measuring the linewidth is a simple way to determine the EPC. This is the Case in graphene, graphite and nanotubes, where  $\gamma^{an}$  is much smaller than  $\gamma^{EP}$  [12].

The EPC contribution to  $\gamma_{\mathbf{q}\eta}$  is given by the Fermi golden rule [24]:

$$\gamma_{\mathbf{q}\eta}^{EP} = \frac{4\pi}{N_{\mathbf{k}}} \sum_{\mathbf{k}, i, j} |g_{(\mathbf{k}+\mathbf{q})j, \mathbf{k}i}|^2 [f_{\mathbf{k}i} - f_{(\mathbf{k}+\mathbf{q})j}] \delta[\epsilon_{\mathbf{k}i} - \epsilon_{(\mathbf{k}+\mathbf{q})j} + \hbar\omega_{\mathbf{q}\eta}], \quad (5)$$

where  $\delta$  is the Dirac distribution,  $g_{(\mathbf{k}+\mathbf{q})j, \mathbf{k}i} = D_{(\mathbf{k}+\mathbf{q})j, \mathbf{k}i} \sqrt{\hbar/(2M\omega_{\mathbf{q}\eta})}$ .

The electron states contributing to the sum in equation (5) are selected by the energy conservation condition  $\epsilon_{\mathbf{k}i} + \hbar\omega_{\mathbf{q}\eta} = \epsilon_{(\mathbf{k}+\mathbf{q})j}$ . Also, the state  $\mathbf{k}i$  has to be occupied and  $(\mathbf{k}+\mathbf{q})j$  empty, so that the term  $[f_{\mathbf{k}i} - f_{(\mathbf{k}+\mathbf{q})j}] \neq 0$ . Thus, only electrons in the vicinity of the Fermi level contribute to  $\gamma^{EP}$ . In insulating and semiconducting systems  $\gamma^{EP} = 0$ . In general, a precise estimate of  $\gamma^{EP}$  from equation (5) is possible only after an accurate determination of the Fermi surface. However, graphene and SWNTs are very fortunate cases. Thanks to their particular band structure,  $\gamma^{EP}$  is given by a simple analytic formula.

The G peak of graphene is due to the  $\Gamma$ -E<sub>2g</sub> phonon [26, 25]. We use equation (5) to compute the width,  $\gamma_{\Gamma}^{EP}$ , for this mode. Close to  $\mathbf{K}$ , we assume the  $\pi$  bands dispersion to be conic from the Fermi level  $\epsilon_F$ , with slope  $\beta$  (figure 3(a)) For both LO and TO modes:

$$\gamma_{\Gamma}^{EP} = \frac{\sqrt{3}a_0^2\hbar^2}{4M\beta^2} \langle D_{\Gamma}^2 \rangle_F. \quad (6)$$

According to equation (6), the EPC  $\langle D_{\Gamma}^2 \rangle_F$  can be directly obtained by measuring the phonon linewidth  $\gamma_{\Gamma}^{EP}$ . Finally, near  $\Gamma$  the conservation of the energy and momentum in equation (5), implies:

$$\gamma_{\mathbf{q}}^{EP} = 0 \Leftrightarrow \mathbf{q} \geq \hbar\omega_{\Gamma}/\beta. \quad (7)$$

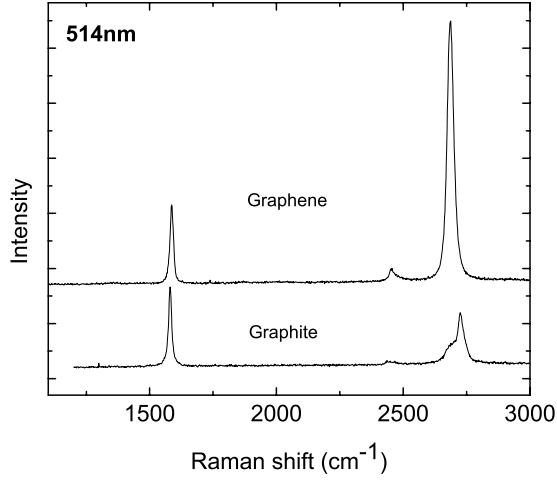


**Fig. 4.** Raman spectra of Graphene and Graphite measured at 514 nm excitation.

This condition is satisfied by the  $E_{2g}$  phonon, involved in the Raman G peak of graphene. Extending to finite  $T$  and  $\epsilon_F \neq 0$  we get [17,18]:

$$\gamma = \frac{\pi^2 \omega_{\Gamma} \alpha'}{c} \left[ f\left(-\frac{\hbar \omega_{\Gamma}}{2} - \epsilon_F\right) - f\left(\frac{\hbar \omega_{\Gamma}}{2} - \epsilon_F\right) \right], \quad (8)$$

where  $c$  is the speed of light and  $\alpha' = 2A_0 \langle D_{\Gamma}^2 \rangle \hbar / (2\pi M \omega_{\Gamma} \beta^2)$ .  $\gamma$  drops to zero for  $\epsilon_F > \hbar \omega_{\Gamma} / 2$  because the scattering process is forbidden by the Pauli exclusion principle.

Equation (5) can also be used to derive the EPC contribution in metallic SWNTs. The EPC of a SWNT can be obtained from the graphite EPC  $\langle D_{\Gamma}^2 \rangle_F$  via zone-folding (valid for  $d \geq 0.8$  nm) [12]. Four scattering processes are involved (figure 3(b)) and for a given tubes diameter  $d$  the LO and TO linewidths are:

$$\gamma_{\Gamma-LO}^{EP} = \frac{2\sqrt{3}\hbar a_0^2 \langle D_{\Gamma}^2 \rangle_F}{\pi M \omega_{\Gamma} \beta d}; \quad \gamma_{\Gamma-TO}^{EP} = 0. \quad (9)$$

Equation (9) is a key result. It shows that the EPC contributes to the linewidth only for the LO mode in metallic SWNTs. For semiconducting SWNTs the EPC contribution is zero for both the TO and LO modes, since the gap does not allow to satisfy the energy conservation in equation (5). Equation (9) can be extended to finite  $T$  in a similar way to equation (8).

## 5 Phonons and Raman spectra of graphene and doped graphene

### 5.1 Pristine graphene and graphene layers

Figure 4 compares the 514 nm Raman spectra of graphene and bulk graphite [25]. The two most intense features are the G peak at  $\sim 1580$   $\text{cm}^{-1}$  and a band at  $\sim 2700$   $\text{cm}^{-1}$ , historically named  $G'$ , since it is the second most prominent band always observed in graphite samples [25]. The G peak is due to the doubly degenerate zone centre  $E_{2g}$  mode [28]. On the contrary, the  $G'$  band has nothing to do with the G peak, but is the second order of zone boundary phonons. Since zone-boundary phonons do not satisfy the Raman fundamental selection rule, they are not seen in the first order Raman spectra of defect-free graphite [27]. Such phonons give rise to a Raman peak at  $\sim 1350$   $\text{cm}^{-1}$  in defected graphite, called D peak [25]. Thus, for clarity, we refer to the  $G'$  peak as 2D. The 2D peak in bulk graphite consists of two components  $2D_1$  and  $2D_2$  [28,27], roughly 1/4 and 1/2 the height of the G peak, respectively. Graphene has a single, sharp 2D peak.

Figure 5 plots the evolution of the 2D band as a function of the number of layers for 514.5 nm excitation [25]. Bi-layer graphene has a much broader and up-shifted 2D band with respect to

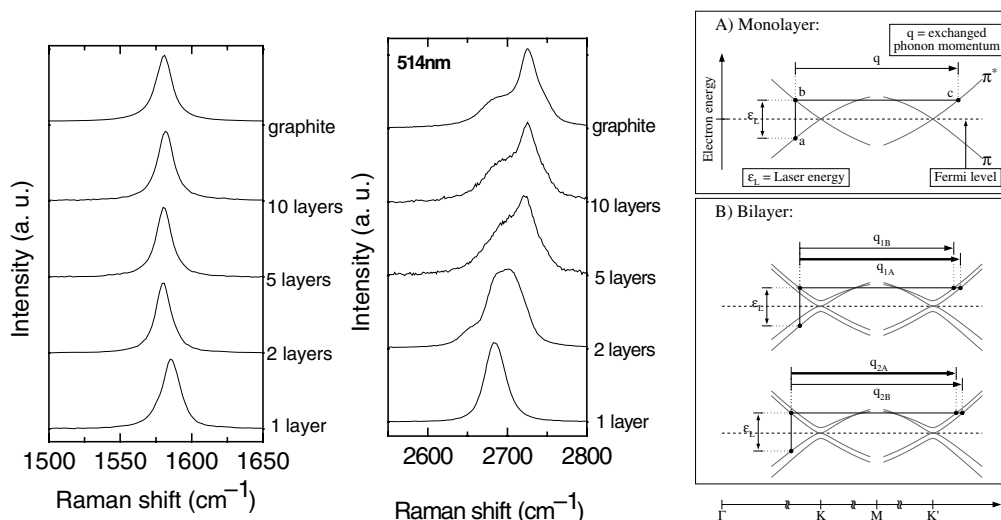


**Fig. 5.** *Left:* Raman spectra of Graphene as a function of number of layers. *Right:* DR for the 2D peak in (A) graphene and (B) bi-layer graphene.

graphene. This band is also quite different from bulk graphite. It has 4 components,  $2D_{1B}$ ,  $2D_{1A}$ ,  $2D_{2A}$ ,  $2D_{2B}$ , 2 of which,  $2D_{1A}$  and  $2D_{2A}$ , have higher relative intensities than the other 2. A further increase of the number of layers leads to a significant decrease of the relative intensity of the lower frequency  $2D_1$  peaks. For more than 5 layers the Raman spectrum becomes hardly distinguishable from that of bulk graphite [26]. On the other hand the shape of the G peak does not change with the number of layers. However, a slight upshift can be seen in the case of graphene. This is due to a combination of self-doping [17], as discussed later, and to the fact that the frequency of the Raman active phonon in graphene is slightly higher than in graphite, due to the mode splitting (see lower panel figure 1, [6]).

The 2D peak in graphene is due to two phonons with opposite momentum in the highest optical branch near  $\mathbf{K}$  [6,25,29]. This peak changes in position with varying excitation energy. This is due to a Double Resonance (DR) process, which links the phonon wave-vectors to the electronic band structure [30].

Within DR, Raman scattering is a fourth order process involving four virtual transitions: i) a laser induced excitation of an electron/hole pair ( $a \rightarrow b$  vertical transition in figure 5(a)); ii) electron-phonon scattering with an exchanged momentum  $\mathbf{q}$  close to  $\mathbf{K}$  ( $b \rightarrow c$ ); iii) electron-phonon scattering with an exchanged momentum  $-\mathbf{q}$  ( $c \rightarrow b$ ); iv) electron/hole recombination ( $b \rightarrow a$ ). The DR condition is reached when the energy is conserved in these transitions. The resulting 2D Raman frequency is twice the frequency of the scattering phonon, with  $\mathbf{q}$  determined by the DR condition [26]. The other two possible DR phonons, with  $q < K$  and  $q \sim K$ , give a much smaller contribution to the Raman intensity. In fact, the  $q < K$  phonon involves a smaller portion of the phase-space because of the band-structure trigonal warping (see figure 4 of [31] and related discussion) and the  $q \sim K$  phonon has a zero electron-phonon coupling for this transition [6]. In the bi-layer, the interaction of the graphene planes causes the  $\pi$  and  $\pi^*$  bands to divide in four bands, with a different splitting for electrons and holes, figure 5(b). Amongst the 4 possible optical transitions, the incident light couples more strongly the two transitions shown in figure 5(b). The two almost degenerate phonons in the highest optical branch couple all electron bands amongst them. The resulting four processes involve phonons with momenta  $q_{1B}$ ,  $q_{1A}$ ,  $q_{2A}$ , and  $q_{2B}$ , as shown in figure 5(b). These wave-vectors correspond to phonons with different frequencies, due to the strong phonon dispersion around  $\mathbf{K}$  induced by the electron-phonon coupling [6]. They produce four different peaks in the Raman spectrum of bi-layer graphene [26].

## 5.2 Doped graphene

By doping graphene, the change in the Fermi surface moves the Kohn anomaly away from  $\mathbf{q} = 0$ . Thus, since Raman probes  $\mathbf{q} = 0$  phonons, intuitively we expect a stiffening of the  $\mathbf{q} = 0$  G peak.

Figure 6 reports the G peak position and FWHM measured at 200 K as a function of electron doping. The G peak upshifts and sharpens with doping [17]. The trends in figure 6 are qualitatively similar to those reported by [32] at 10 K.

The  $E_{2g}$  phonon in graphene consists of an in-plane displacement of the carbon atoms by a vector  $\pm \mathbf{u}/\sqrt{2}$ . In presence of such atomic displacements, the bands are still described by a cone (i.e. a gap does not open) with the Dirac-point shifted from  $\mathbf{K}$  by a vector  $\mathbf{s}$  [17, 33]. In practice, the atomic-pattern of the  $E_{2g}$  vibrations is mirrored into an identical pattern of Dirac-point vibrations in the reciprocal space. The dependence of the electronic-bands on  $\mathbf{u}$  is [17]:

$$\epsilon(\mathbf{k}, \pi^*/\pi, \mathbf{u}) = \pm \hbar v_F |\mathbf{k} - \mathbf{s}(\mathbf{u})|, \quad (10)$$

where  $\mathbf{s} \cdot \mathbf{u} = 0$ ,  $s = u \sqrt{2 \langle D_{\Gamma}^2 \rangle_F} / (\hbar v_F)$ .

The knowledge of the electronic-bands (in the presence of a phonon) allows the determination of the phonon energy  $\hbar \omega_{\epsilon_F}$  as a function of  $\epsilon_F$ . In particular,

$$\hbar \Delta \omega = \hbar \omega_{\epsilon_F} - \hbar \omega_0 = \frac{\hbar}{2M\omega_0} \frac{d^2 \Delta E}{(du)^2}, \quad (11)$$

where  $M$  is the carbon mass,  $\omega_0$  is the frequency in the undoped case,  $\Delta \omega \ll \omega_0$  and  $\Delta E$  is the variation of the electronic energy with  $\epsilon_F$ .

Within the adiabatic Born–Oppenheimer approximation,  $\Delta E(u)$  is computed assuming a static atomic displacement. Under this hypothesis, for any given displacement  $\mathbf{u}$ , the electrons are supposed to be in the ground state, i.e. the bands are filled up to  $\epsilon_F$ . Thus, the adiabatic  $\Delta E$  is:

$$\Delta E(u) = \frac{4A}{(2\pi^2)} \int_{\epsilon(\mathbf{k}, \pi^*, \mathbf{u}) < \epsilon_F} \epsilon(\mathbf{k}, \pi^*, \mathbf{u}) d^2 k, \quad (12)$$

where we consider  $\epsilon_F > 0$ ,  $A = 5.24 \text{ \AA}^2$  is the unit-cell area, a factor 4 accounts for spin and  $\mathbf{K}$ -point degeneracy. Combining equations (10) and (12), we have that  $\Delta E$  does not depend on  $\mathbf{u}$  and  $\hbar \Delta \omega = 0$ . Thus, within the adiabatic approximation, the Raman G peak position is independent of  $\epsilon_F$ , in contrast with experiments, figure 6.

The experimental results are explained considering non-adiabatic contributions to the dynamical matrix, as for equation (3) [18, 34, 35]. At  $T = 0$  the G peak shift can be described analytically [18]:

$$\hbar \Delta \omega = \frac{\hbar A \langle D_{\Gamma}^2 \rangle_F}{\pi M \omega_0 (\hbar v_F)^2} \left[ |\epsilon_F| + \frac{\hbar \omega_0}{4} \ln \left( \frac{|\epsilon_F| - \frac{\hbar \omega_0}{2}}{|\epsilon_F| + \frac{\hbar \omega_0}{2}} \right) \right]. \quad (13)$$

The result of equation (13) can be extended to any  $\epsilon_F$  and finite temperature  $T$  by computing the real part of the phonon self energy with the DFT electron–phonon coupling matrix-elements to obtain [17, 18]:

$$\hbar \Delta \omega = \alpha' P \int_{-\infty}^{\infty} \frac{[f(\epsilon - \epsilon_F) - f(\epsilon)] \epsilon^2 \text{sgn}(\epsilon)}{\epsilon^2 - (\hbar \omega_0)^2/4} d\epsilon, \quad (14)$$

where  $P$  is the principal part [18, 34, 35]. Figure 6 shows the excellent agreement of the non-adiabatic finite  $T$  calculation (equation (14)) with the experiments.

By comparing the adiabatic and non-adiabatic calculations, we conclude that the stiffening of the  $E_{2g}$  mode with  $|\epsilon_F|$  is due to the departure of the electron population from the adiabatic ground state [17].

This is further confirmed by the analysis of the G peak linewidth. From equations (6), (8). At  $T = 0$ ,  $\gamma^{an} = 11 \text{ cm}^{-1}$  for  $\epsilon_F = 0$  and  $\gamma^{an}$  drops to zero for  $\epsilon_F > \hbar \omega_0/2$  because the scattering

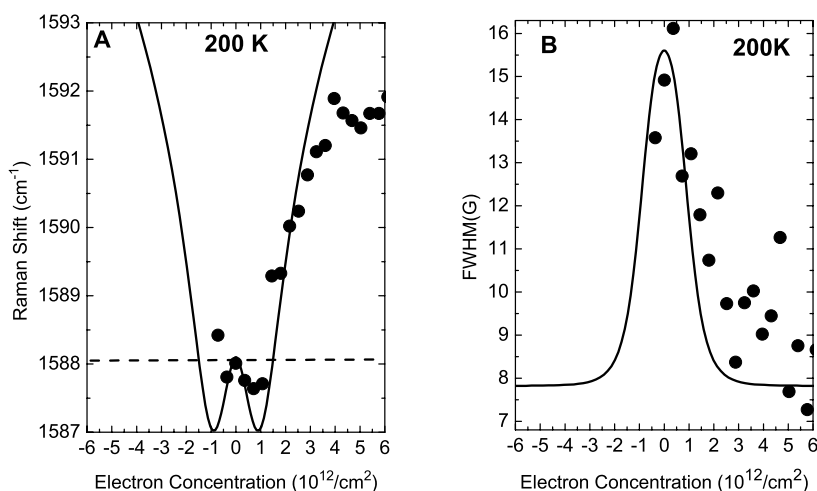


**Fig. 6.** (A) G peak position as a function of electron concentration at 200 K. (dots) measurements; (horizontal-dashed line) adiabatic Born-Oppenheimer; (line) finite-temperature non-adiabatic calculation from equation (14). The minimum observed in the calculations at  $\sim 10^{12} \text{ cm}^{-2}$  occurs when the Fermi Energy equals half of the phonon energy. (B) FWHM(G) at 200 K as a function of electron concentration (dots) measured; (line) theoretical FWHM of a Voigt profile obtained from a Lorentzian component given by equation (8), and a constant Gaussian component of  $\sim 8 \text{ cm}^{-1}$  [17].

process is forbidden by the Pauli exclusion principle [12]. Figure 6(b) shows a good agreement between the experimental and theoretical FWHM(G), once a constant inhomogeneous Gaussian broadening of  $\sim 8 \text{ cm}^{-1}$  is added to the electron-phonon contribution of equation (8) [17].

Interestingly, in SWNT, due to the reduced dimensionality, even for the undoped case the non-adiabatic contributions are essential to describe the phonons [13]. More so in the case of doped SWNT [36].

## 6 Phonons and Raman spectra of SWNTs

In SWNTs, the double degenerate Raman active  $E_{2g}$  mode of graphene splits into two distinct phonons. As shown in figure 7, such modes are polarized respectively along the tube axis (longitudinal mode) and along the tube circumference (tangential mode), and are usually referred to as the LO and the TO modes [13].

In the  $1550\text{--}1590 \text{ cm}^{-1}$  region, the Raman spectra of SWNTs are characterized by the presence of two distinct features: the so called  $G^+$  and  $G^-$  peaks. These peaks are due to the LO and TO modes, and their shape and position strongly depend on the electronic properties of the tubes. The  $G$  band of a metallic and of a semiconducting SWNT [37] are compared in figure 7. In semiconducting tubes, both the  $G^+$  and the  $G^-$  peaks appear as sharp Lorentzians, centered respectively at  $\sim 1590 \text{ cm}^{-1}$  and  $1570 \text{ cm}^{-1}$ . The  $G^+$  peak is usually more intense than the  $G^-$ , and its position is substantially independent of the tube's diameter, whereas the position of the  $G^-$  peak decreases for decreasing tubes diameter. On the other hand, in metallic tubes, the  $G^-$  peak is usually rather intense, very broad, and sensibly downshifted with respect to its counterpart in semiconducting tubes.

In semiconducting tubes, the splitting between the LO and the TO mode is usually explained in terms of curvature. Indeed, the  $\sigma-\pi$  mixing of the C-C bonds along the circumference results in a softening of the TO mode with respect to the LO, accounting for both the peaks splitting and the diameter dependence of the  $G^-$  position.

For metallic tubes, different theories have been proposed. The first attempt to explain the broadened, downshifted  $G^-$  in metallic SWNTs was based on a Fano resonance between the TO phonon and the plasmons in metallic tubes [38, 39]. However, this model is in poor agreement

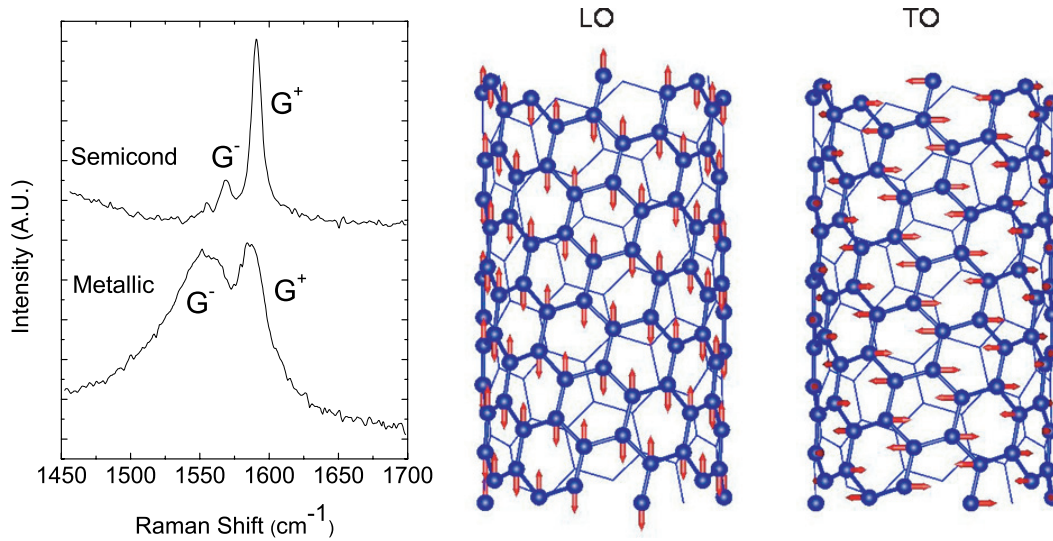


**Fig. 7.** *Right:* Raman  $G$ -band of semiconducting and metallic SWNTs. Semiconducting tubes are characterized by two sharp peaks. Metallic tubes show a characteristic broad, downshifted  $G^-$  peak (adapted from [37]). *Left:* LO and TO phonon modes of SWNTs derived from the  $E_{2g}$  phonon of graphene.

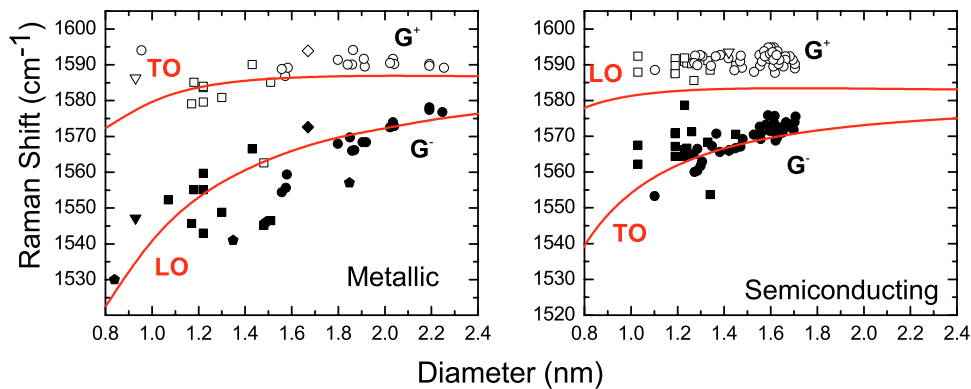


**Fig. 8.** Comparison between the computed frequency of the LO and the TO phonon in SWNTs and the position of the  $G^+$  and the  $G^-$  Raman peak in metallic and semiconducting tubes. Calculations include the dynamic effects and a correction for the curvature effects [13].

with the experimental results, and neglects both the presence of Kohn anomalies in the phonon dispersion of metallic SWNTs, and the role of the electron–phonon interaction. Indeed, it is possible to prove by means of the EZF calculations described in section 3, that the  $G^-$  peak of metallic SWNTs is strongly shaped by the effects of the electron–phonon coupling [12,13]. Modeling the EPC in metallic SWNTs by using the same tight binding model used for graphene, it is possible to show that the EPC affects the LO mode only. The EPC acts on the LO mode in two different ways. First, it is responsible for the onset of a Kohn anomaly resulting in a strong downshift of the LO frequency. Second, in agreement with the Fermi golden rule, it reduces the LO phonon lifetime, resulting in an increase of the phonon linewidth. Thus, in metallic tubes the  $G^-$  peak is not originating from a curvature-downshifted TO phonon, like in semiconducting tubes, but derives from an EPC-affected LO mode [12,13].

The prediction given by the dynamic, time-dependent, model can be compared with the data from Raman spectroscopy. Figure 8 shows that the computed frequencies of the TO and LO modes in metallic SWNTs are in excellent agreement with the position of the  $G^+$  and  $G^-$

Raman peaks. Thus we assign the  $G^+$  and  $G^-$  peaks of metallic nanotubes to TO (tangential) and LO (axial) modes, the opposite of semiconducting nanotubes [12,13].

The non-adiabatic Kohn anomaly at  $\Gamma$  also explains the observed electronic temperature dependence of the Raman spectra [13].

## 7 Conclusions

We reviewed the phonon dispersions of graphene, showing the presence of two Kohn anomalies induced by the strong electron–phonon coupling of the  $E_{2g}$  mode at  $\Gamma$  and the  $A'_1$  mode at  $\mathbf{K}$ . The Kohn anomalies in metallic SWNTs have to be described by using an approach accounting for the time-dependent nature of phonons, usually neglected in the common Born–Oppenheimer framework. The same applies in the case of doped graphene.

S.P. acknowledges funding from Pembroke College Cambridge. A.C.F. from The Royal Society and The Leverhulme Trust.

## References

1. K.S. Novoselov, D. Jiang, F. Schedin, T.J. Booth, V.V. Khotkevich, S.V. Morozov, A.K. Geim, Proc. Natl. Acad. Sci. USA **102**, 10451 (2005)
2. K.S. Novoselov, A.K. Geim, S.V. Morozov, D. Jiang, Y. Zhang, S.V. Dubonos, I.V. Grigorieva, A.A. Firsov, Science **306**, 666 (2004)
3. R. Saito, G. Dresselhaus, M.S. Dresselhaus, *Physical Properties of Carbon Nanotubes* (Imperial College Press, London, 1998)
4. S. Reich, C. Thomsen, J. Maultzsch, *Carbon Nanotubes: Basic Concepts and Physical Properties* (Wiley-VCH, Weinheim, 2004)
5. A.C. Ferrari, J. Robertson (eds.), Phil. Trans. Roy. Soc. A **362**, 2267 (2004)
6. S. Piscanec, M. Lazzeri, F. Mauri, A. Ferrari, J. Robertson, Phys. Rev. Lett. **93**, 185503 (2004)
7. J.P. Perdew et al., Phys. Rev. Lett. **77**, 3865 (1996)
8. S. Baroni et al., Rev. Mod. Phys. **73**, 515 (2001)
9. N. Troullier, J.L. Martins, Phys. Rev. B **43**, 1993 (1991)
10. M. Methfessel, A.T. Paxton, Phys. Rev. B **40**, 3616 (1989)
11. W. Kohn, Phys. Rev. Lett. **2**, 393 (1959)
12. M. Lazzeri, S. Piscanec, F. Mauri, A.C. Ferrari, J. Robertson, Phys. Rev. B **73**, 155426 (2006)
13. S. Piscanec, M. Lazzeri, J. Robertson, A.C. Ferrari, F. Mauri, Phys. Rev. B **75**, 035427 (2007)
14. M. Lazzeri, S. Piscanec, F. Mauri, A.C. Ferrari, J. Robertson, Phys. Rev. Lett. **95**, 236802 (2005)
15. J. Maultzsch, S. Reich, C. Thomsen, H. Requardt, P. Ordejón, Phys. Rev. Lett. **92**, 075501 (2004)
16. V. Zolyomi, J. Kurti, Phys. Rev. B **70**, 085403 (2004)
17. S. Pisana, M. Lazzeri, C. Casiraghi, K.S. Novoselov, A.K. Geim, A.C. Ferrari, F. Mauri, Nat. Mat. **6**, 198 (2007)
18. M. Lazzeri, F. Mauri, Phys. Rev. Lett. **97**, 266407 (2006)
19. M. Born, R. Oppenheimer, Ann. Phys. **84**, 457 (1927)
20. S. de Gironcoli, Phys. Rev. B **51**, 6773 (1995)
21. P.B. Allen, *Dynamical Properties of Solids*, edited by G.K. Horton, A.A. Maradudin (North-Holland, Amsterdam, 1980), Vol. 3, p. 95
22. K.P. Bohnen, R. Heid, H.J. Liu, C.T. Chan, Phys. Rev. Lett. **93**, 245501 (2004)
23. D. Connetable, G.M. Rignanese, J.C. Charlier, X. Blase, Phys. Rev. Lett. **94**, 015503 (2005)
24. P.B. Allen, Phys. Rev. B **6**, 2577 (1972); P.B. Allen, R. Silbergliitt, *ibid.*, **9**, 4733 (1974)
25. A.C. Ferrari, J.C. Meyer, V. Scardaci, C. Casiraghi, M. Lazzeri, F. Mauri, S. Piscanec, D. Jiang, K.S. Novoselov, S. Roth, A.K. Geim, Phys. Rev. Lett. **97**, 187401 (2006)
26. F. Tuinstra, J. Koenig, J. Chem. Phys. **53**, 1126 (1970)
27. R.P. Vidano, D.B. Fishbach, L.J. Willis, T.M. Loehr, Solid State Commun. **39**, 341 (1981)
28. R.J. Nemanich, S.A. Solin, Phys. Rev. B **20**, 392 (1979)
29. A.C. Ferrari, J. Robertson, Phys. Rev. B **61**, 14095 (2000)
30. C. Thomsen, S. Reich, Phys. Rev. Lett. **85**, 5214 (2000)

31. J. Kurti, V. Zolyomi, A. Gruneis, H. Kuzmany, *Phys. Rev. B* **65**, 165433 (2002)
32. J. Yan, Y. Zhang, P. Kim, A. Pinczuk, *cond-mat/0612634* (2006)
33. O. Dubay, G. Kresse, *Phys. Rev. B* **67**, 035401 (2003)
34. T. Ando, *J. Phys. Soc. Jpn.* **75**, 124701 (2006)
35. A.H. Castro Neto, F. Guinea, *Phys. Rev. B* **75**, 045404 (2007)
36. N. Caudal, A.M. Saitta, M. Lazzeri, F. Mauri, *cond-mat/0702493* (2007)
37. A. Jorio, R. Saito, M.S. Dresselhaus, G. Dresselhaus, *Trans. Roy. Soc. A* **362**, 2311 (2004)
38. S.D.M. Brown, A. Jorio, P. Corio, M.S. Dresselhaus, G. Dresselhaus, R. Saito, K. Kneipp, *Phys. Rev. B* **63**, 155414 (2001)
39. K. Kempa, *Phys. Rev. B* **66**, 195406 (2002)